# Device design and flow scaling for liquid sheet jets

Byunghang Ha (하병항),[1] Daniel P. DePonte,[2] and Juan G. Santiago[1,*]
[1]*Department of Mechanical Engineering, Stanford University, Stanford, California 94305, USA*
[2]*Linac Coherent Light Source, SLAC National Accelerator Laboratory, Menlo Park, California 94025, USA*

(Received 9 February 2018; published 20 November 2018)

We present a design and experimental study of microfluidic converging nozzles which creates a stable liquid sheet jet. The sheet jets formed by the nozzles can be varied between order 10 $\mu$m to submicron thicknesses (a measured minimum thickness of 560 nm). A parametric study of the jet structure was performed including 51-fold variation of Reynolds number, 20-fold variation of Weber number, 89-fold variation of capillary number, and 12-fold variation of nozzle exit aspect ratio. These studies benefited from variation of working liquids, nozzle geometry, 10-fold variation of flow rate, and 7.1-fold variation of key length scales. Navier-Stokes simulations of internal fluid flow were also performed to identify key physical phenomena. These studies were used to propose and test physical scaling theories for jet thickness, length, and width of the primary sheet. The scaling theories are also informed by classic studies of colliding jets with similar flow structures. For sheet thickness, we present two scaling approaches: one relying on internal fluid flow calculations and the other based solely on nozzle geometry. For sheet length and width, scaling theories are presented based on the nozzle geometry and essential dimensionless flow parameters. The scalings do not require numerical simulation of external flow and exhibit efficient collapse across the parameter space. Together, the fabrication method and scaling theories provide a clear path to the rapid and efficient design of liquid sheet jets.

DOI: 10.1103/PhysRevFluids.3.114202

## I. INTRODUCTION

Liquid sheet jet formation is a fundamental free-surface fluid mechanics phenomenon which has received significant attention. The classical and by far the most popular method of forming flat sheets of liquid is by colliding two identical cylindrical liquid jets at an oblique angle [1–3]. For example, Taylor created thin lenticular sheets of water by colliding two jets obliquely and measured the shapes and thickness distribution of the sheets [2]. He used potential flow principles and force balance equations to estimate sheet distributions of sheet thickness as a function of the downstream coordinate and compared these predictions to experimentally obtained sheet jet images. Since that seminal work, there have been numerous studies over the last five decades, and these have sought to describe flow regimes and structures of colliding jets, as reviewed by Clanet [4]. Notable work includes that of Bush and Hasha, who investigated sheet structures made by colliding jets of liquids with dynamic viscosities of approximately 10–100 times that of water, in part to create jets with stable sheet rims [3]. By increasing the viscosity of the test liquid, they accessed and investigated parameter regimes characterized by stable rims.

Devices which produce stable liquid sheets of order 1 $\mu$m and submicron thicknesses are enabling unique experimental spectroscopy and structural biology studies [5–9]. For example, liquid sheet jets are used for sample delivery into x-ray free electron lasers, synchrotrons, and pulsed

*juan.santiago@stanford.edu

 

electron facilities which offer unprecedentedly rapid temporal and spatial resolution [10] as well as time-resolved soft x-ray absorption or transmission spectroscopy [6,11,12]. Other examples of liquid sheets include a wire-guided sheet jet for resonance Raman and optical absorption spectroscopy [8], an impinging jet on a flat surface for a short-cavity dye laser [13], and a slit jet for dye laser and tetrahertz spectroscopy [5,9]. There are several major reasons for these uses and applications of sheet jets. First, thin sheet jets freely flowing in air or under vacuum can minimize background scattering and mitigate fouling problems associated with thin (internal) flows in enclosed channels [10]. The feature of a free liquid structure (no channel walls near probing site) is particularly important for samples analyzed using free electron lasers (FELs) for which the incident x-ray intensity can be sufficiently high to destroy virtually any kind of channel material. Second, jet fluid speeds are typically on the order of tens of meters per second and so provide rapid introduction of sample compatible with high-repetition-rate, pulsed probes. The associated fast replenishment enables probing of sample material only once per probe pulse. Third, sheet jets can be made with order 1 μm thicknesses helping to minimize any unwanted background signal from the liquid when used as a sample carrier [6,7,12]. Fourth, sheet jets offer a significant target area in comparison to cylindrical jets of similar thickness, an important consideration for a broad range of spectroscopy applications, as reviewed by Ghazal *et al.* [10]. When used in pump-probe experiments, sheets facilitate alignment and allow for a uniform sample pump illumination without the lensing effects caused by curved liquid surfaces of cylindrical jets or drops. This is similarly important for reducing optical distortion associated with cylindrical jets for imaging studies [5,7]. Finally, fast hydrodynamic focusing and other rapid mixing strategies can be incorporated upstream of sheet jet generation for fast reaction studies [10,14].

In this paper, we present a microfluidic device design which is convenient for the generation of sheet jets. The device is easier to implement than a two-nozzle colliding jet setup, as it uses a symmetric flow passage with a single nozzle and exit port. The sheet jet is created from a single stream of liquid flowing through a converging channel with a rectangular cross section and nozzle aperture. We also present an easy-to-reproduce fabrication method which enables fast prototyping and simple operation and readily lends itself to standard soft and hard lithography chip fabrication methods. Our sheet jet study was based on experiments performed only in ambient air, and our work would likely be useful in hard x-ray spectroscopy and many FEL pump-probe experiments, which are often performed in air. Galinis *et al.* very recently used a single nozzle device with a different geometry to demonstrate stable sheet jets in atmosphere and under vacuum [7]. Using interferometric imaging to quantify sheet jet thicknesses, Galinis *et al.* showed thickness profiles were very similar for jets created in ambient atmosphere versus in vacuum. This suggests that our device and scaling theories validated in air may similarly work under vacuum.

We present an experimental study wherein we perform parametric variations of nozzle geometry, flow rate, and fluid properties (viscosity and surface tension in particular). We performed full Navier-Stokes simulations of the internal flow of the devices and used these results to form hypotheses regarding the flow structure of the external free jet. We use these experimental and numerical data to propose and identify dimensionless parameters and physical scaling relations which collapse the experimentally observed sheet thickness, length, and width dimensions across the entire range of our experiments. We vary internal flow Reynolds number from 74.7 to 3820 (using applied pressures between 338 and 8690 kPa), Weber numbers from 188 to 3700, and capillary numbers from 0.0578 to 5.15 including 3.3-fold variation of surface tension and 9.7-fold variation of dynamic viscosity. We find that crucial jet sheet dimensions such as sheet thickness and in-plane sheet length and width can be largely predicted solely from nozzle geometry (including aspect ratio and convergence angle), bulk flow rate, and thermophysical parameters (including density, surface tension, and dynamic viscosity). Our results enable rapid design and selection of sheet jets among various applications without the need for detailed flow simulation and experimental parametric studies. The results also highlight the crucial role of nozzle geometry, spanwise-to-streamwise momentum flux ratio, Weber number, and capillary number on minimum sheet thickness, in-plane width, and usable sheet streamwise length.

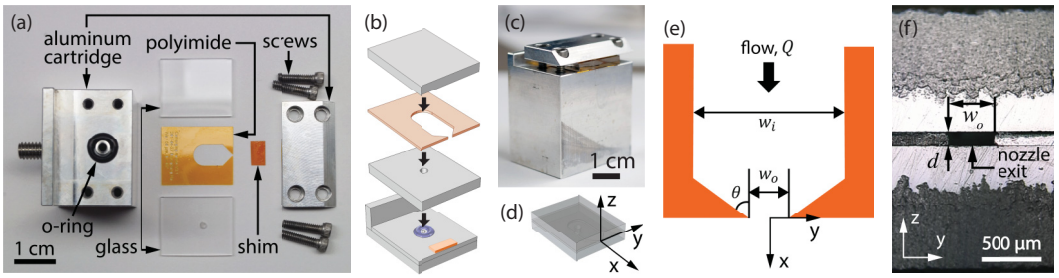


FIG. 1. Microfluidic device design for the reproducible generation of liquid sheet jets. (a) Image of disassembled device. (b) Exploded schematic view of the planar design and connection ports (fasteners not shown). (c) Image of a fully assembled nozzle. (d) Top portion of assembly and Cartesian coordinates. (e) Schematic top view of microfluidic channel describing flow and geometric parameters. (f) Optical micrograph of a polished nozzle exit.

## II. METHODS AND MATERIALS

### A. Sheet jet device design

We aimed to design a monolithic device that is easy to operate. The device obviates a need of alignment and operation control of two independent colliding jets. The device also lends itself to easy-to-reproduce fabrication methods and an easy-to-replace chip and cartridge module system.

Our microfluidic device design and assembly is described in Fig. 1 and includes three layers: top channel wall (glass), channel (polyimide film), and bottom channel wall with an inlet port (glass). The components of Fig. 1(a) were assembled as a stack [Figs. 1(b)–1(d)]. The O ring provided the seal between the bottom glass layer to the aluminum body [bottom of Fig. 1(b)]. The seal between the glass slides and polyimide required no adhesives. Screws passed through countersunk holes on a top plate and mated with female threads on the bottom block compress and seal all parts of the assembly [Fig. 1(c)]. A 127 $\mu$m-thick polyimide shim was inserted between the glass and aluminum [Figs. 1(a) and 1(b)] to improve the clamping pressure at the nozzle exit. The nozzle exit was rectangular with a controllable aspect ratio [Fig. 1(f)]. We defined the origin of our coordinates at the center in the cross-sectional plane of the nozzle exit as shown in Figs. 1(d)–1(f). Key parameters for the channel geometry and the flow condition are summarized in Figs. 1(e) and 1(f): flow rate ($Q$), nozzle outlet width ($w_o$), convergence angle ($\theta$), and nozzle depth ($d$). Nozzle inlet width ($w_i$) was in all cases much larger than $w_o$ and fixed at 5 mm. For our parametric studies, we varied $Q$, $w_o$, $d$, and $\theta$, respectively, as follows: 6–60 ml/min, 150–1065 $\mu$m, 38–125 $\mu$m, and 45–85°.

### B. Fabrication and operation

The three layers comprising the microfluidic chips were fabricated via UV laser ablation (3W diode pumped solid state laser, DPSS Lasers, Inc., CA, USA). The top and bottom layers were made out of 500 $\mu$m-thick microscopic glass slides. The middle layer was made out of commercially available polyimide films (150MT, 200HN, 300HN, and 500HN Kapton® Film, American Durafilm Co., MA, USA). Despite careful alignment during assembly, the three stacked layers were often slightly misaligned resulting in an uneven nozzle exit, that is, the edge of one or two of the layers protruded by more than ∼10 μm past the other(s). Slightly uneven edges near the nozzle face can result in macroscopic asymmetries and imperfections (e.g., visible capillary waves) in the sheet jet structures.

We therefore ground and polished the edges of the device after assembly and tightening of the fasteners. We used 600 to 2400 grit sand papers on a wheel grinder to remove material and polish the surfaces near the nozzle exit. We stress this polishing was very important for reproducible and desired jet sheet shapes.

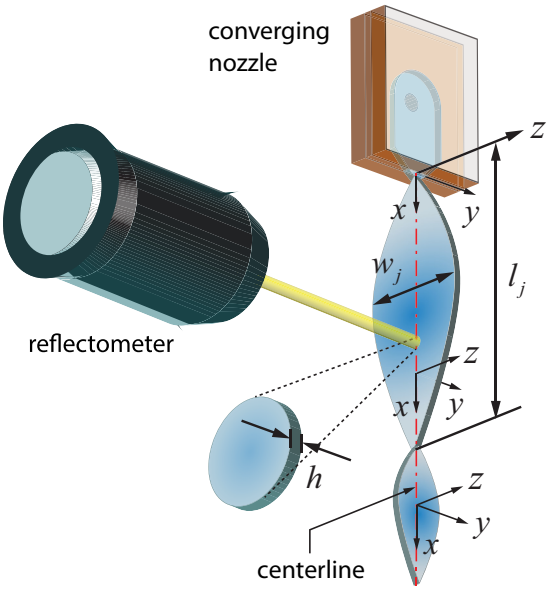


FIG. 2. Schematic illustrating measurement of jet dimensions. Note the primary jet sheet (or the first jet "link" in the chain of links) is oriented at right angle to the plane of the converging nozzle. Subsequent jet links are oriented at right angles to the preceding links. Depicted here is a jet which remains stable from the jet nozzle to the apex (at $x = l_j$) and through the second link. Jet "rims" bounding the sheets are not shown here.

After polishing, the surface at around the nozzle exit was made hydrophobic by spray coating with commercially available window water-repellent treatment (Rain-X®, ITW Global Brands, TX, USA). The polishing and surface treatment dramatically reduced a drip mode wherein order millimeter diameter drops form, grow, and drip down the surfaces of the device and interfere with jet formation. These drops are highly undesirable as they can affect jet structure and result in intermittent and random jetting behavior.

Working liquids were pumped by HPLC pump (LC-20AP, Shimadzu Co., Kyoto, Japan) and delivered to nozzles via conventional HPLC tubing and fittings. To reduce cyclic pressure fluctuations, a 150 ml stainless steel chamber (316L-50DF4-150-PD, Swagelok, CA, USA) was inserted into the delivery line between the pump and nozzle. Air trapped in this "dampener" kept the pressure sufficiently constant that cyclic variation sheet dimensions were negligible. Note the highest flow rates of the most viscous liquid and smallest jet nozzles required total pressure drop of 8690 kPa through the system leaving at minimum about a 2 ml volume of compressed air in the dampener.

### C. Experimental measurements

The sheet jet thickness, $h$, was measured along the axial centerline using a spectral reflectometer (F20, Filmetrics, CA, USA) as illustrated in Fig. 2. The nozzle was oriented so that the jet flowed vertically downward. We used published values for the refractive index of the working liquids [15,16]. We define jet length, $l_j$, is the axial distance from the nozzle exit to the apex of the primary sheet (assuming the entire first oval structure is stable). Jet width, $w_j$, is the largest width of the primary sheet including the diameters of the both rims at the edges. We moved the focused spotlight of the reflectometer probe using optomechanical stages to measure distances: from nozzle exit to the apex of the primary sheet for $l_j$ and largest edge-to-edge width including both rims for $w_j$. We present data for the first link of these jets and were able to measure jet length $l_j$ and width $w_j$ in all cases.

### D. Measurement uncertainty

The bulk of our measurements were performed on the primary jet sheets and quantified their thickness, length, and width. Each sheet thickness, $h$, was obtained from an average of 30 to 80 thickness measurements. Each of these was determined based on measured reflected light intensity data using the spectral reflectometer. To estimate uncertainty of jet thickness, we performed statistical analyses on the individual measurements of these. For the measurements when using ethanol and the mixture of ethylene glycol and water, we found standard deviations of measured sheet thickness were mostly less than 0.1%, at most 0.5%. For the measurements of water jet sheet thickness, the standard deviations of the measured data were mostly less than 1.0%, at most 5.0%.

We measured vertical displacement of the beam spot from nozzle exit to the apex for the sheet length and lateral displacement across the minor axis of the oval for the sheet width, and thus the measurement uncertainty is directly associated with the spot size of the focused probe beam. We estimate the measurement errors of larger dimensions $l_j$ and $w_j$ to be on the order of hundreds of microns.

In the experiments, we controlled flow rate using the HPLC pump (LC-20AP, Shimadzu Co., Kyoto, Japan). We monitored that upstream pump pressures were constant to within 3% for the water and ethanol jets and 5% for the mixture of ethylene glycol and water jets. We analyzed videos for order 10 s scales and observed little fluctuation.

As described in Sec. II B, we used UV laser ablation to cut the geometry of the nozzles in 38 to 127 μm-thick layers of polyimide with nozzle exit widths between 150 and 1065 μm. In order to confirm nozzle dimensions after device assembly, including alignment and polishing, we measured the nozzle outlet depth and width under microscope using a microruler. The values of $d$ and $w_o$ measured are correct to within about $\pm 1$ μm and about $\pm 10$ μm, respectively. The nozzle angle was controlled by the automated positioning of the UV laser ablation system, and we expect those angles are within $\pm 1^\circ$ uncertainty.

### E. Numerical simulation

Velocity fields in the plane of nozzle exit were obtained from full 3D Navier-Stokes numerical simulation using a commercial CFD software, COMSOL (COMSOL, Inc., MA, USA). The domain was a quadrant volume inside the microfluidic nozzles with symmetry conditions about the $x$-$z$ and $x$-$y$ planes. The inlet boundary condition was the fully developed 2D laminar incompressible channel flow given a constant flow rate [17]. The outlet boundary condition was constant zero gauge pressure. An example with ethanol, $Q = 20\,\mathrm{ml/min}$, $w_i = 5\,\mathrm{mm}$, $w_o = 380\,\mu\mathrm{m}$, and $d = 125\,\mu\mathrm{m}$ is shown in Fig. 3. Figure 3(a) shows a 3D contour of static pressure, and Fig. 3(b) shows an arrow plot for velocity vector fields in the $y$-$z$ plane at the nozzle exit. Velocity components for each Cartesian coordinate at a node in the plane of nozzle exit are denoted by $u\,(x = 0,\ y,\ z)$, $v\,(x = 0,\ y,\ z)$, and $w\,(x = 0,\ y,\ z)$, respectively.

## III. SCALING ANALYSIS

We informed our scaling analyses from fluid dynamics insights drawn in part from some colliding jet research including the seminal work of Taylor [2] and Bush and Hasha [3]. First, consider the problem of scaling the $y$-direction thickness of the primary liquid sheet in the $x$-$z$ plane centered at $y = 0$. We here hypothesize that the primary dynamics governing sheet thickness is the conversion of $x$-$y$ plane momentum flux within the nozzle to $x$-$z$ momentum flux outside of the nozzle (the latter acting to stretch the sheet in the $x$-$z$ plane). This hypothesis of approximately inviscid momentum flux development (potential flow) was first applied by Taylor for colliding jets [2].

A good starting point for estimation of colliding jet sheet thickness is Taylor's assumption that, significantly far away from the collision region, jet thickness, $h$, scales inversely with radial distance, $r$. He assumed the flow sufficiently far from the zone of impact was very nearly radial and a simple Euler equation argument leads to a constant radial velocity, $u_0$. This assumption was later verified

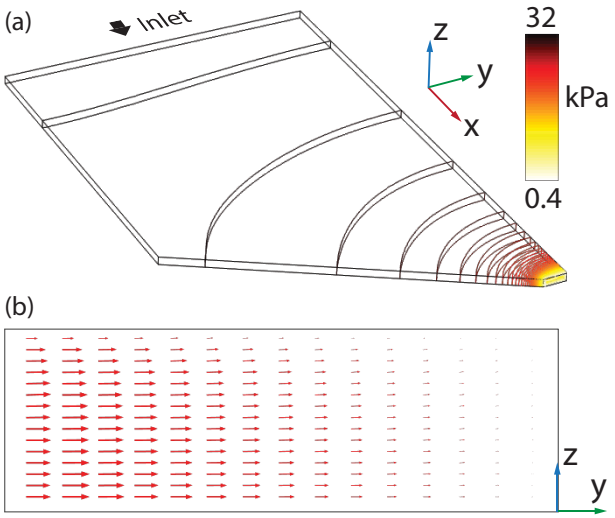


FIG. 3. Numerical simulation for velocity fields at the nozzle exit. (a) Contour of static pressure inside a quadrant of a microfluidic nozzle channel. (b) Arrow plot for velocity fields in the $y$-$z$ plane at the nozzle exit. The largest arrow shown for this case corresponds to a velocity magnitude of 5.88 m/s.

by the particle and bubble tracking experiments of Bush and Hasha, who estimated $u_0$ is constant within about 10% [3]. As a result, from simple mass conservation, they show that $hru_0 = Q(\phi)$, where $Q(\phi)$ is a characteristic parameter (with units of volume flux) which is defined to vary along the azimuthal angle in the plane of the sheet, $\phi$. Assuming $Q(\phi)$ is proportional to the volume flow rate $Q = 2A_j u_0$ with $A_j$ the cross-sectional area of each nozzle, we may write $hr \propto A_j$. Similar relations treating sheet jet thickness, $h$, as proportional to the cross-sectional area of upstream colliding jets and as scaling inversely with radial distance, $r$, have also been used to develop analytical relations describing thickness of sheets resulting from colliding jets [18–20]. Applying similar reasoning to a liquid sheet produced by a converging nozzle suggests $hx \propto A_e$ where $A_e = dw_o$ is the nozzle exit area.

Next, in the classical problem of colliding jets, the important momentum flux components are the (parallel) streamwise and (opposing) transverse components of the jets. By analogy, we here consider the streamwise and spanwise momentum fluxes of the internal flow at the nozzle exit, defined locally by the quantities $\rho u^2$ and $\rho v^2$, respectively. Here $u$ and $v$ are the (nonuniform) velocity components of the flow inside the nozzle. We computed the normal area integral of these using full Navier-Stokes simulations of the internal flow (no free surfaces) using COMSOL (COMSOL, Inc., MA, USA) as described in Sec. II E including Fig. 3. We define the ratio of these spanwise and streamwise integral quantities as $\beta = \sqrt{(\int_{A_e} v^2 dA)/A_e}/\sqrt{(\int_{A_e} u^2 dA)/A_e} = v_{\text{rms}}/u_{\text{rms}}$.

Note that the nozzle exit flow is not purely axial, and the spanwise flow is critical to the spreading and development of the free jet. However, for simplicity, these simulations approximated the exit plane of the nozzle as a zero gauge pressure boundary condition. Similarly as with colliding jets, we here include the influence of momentum flux distribution on sheet thickness as a function of the momentum flux ratio beta, $hx \propto dw_o g(\beta)$.

Last, we recognize that our nozzle geometry is significantly different from the upstream geometry of two colliding cylindrical jets. Accordingly, we hypothesize that the analogous "collision region" occurs somewhere near our nozzle exit. We also recognize that the nozzle geometry significantly influences the downstream radial distribution of jet thickness. We hypothesized that we can capture the influence nozzle geometry by introducing some function of the aspect ratio of the nozzle exit, $\alpha = d/w_o$. Combining these ideas, we hypothesized a generalized nondimensional expression for

sheet thickness:

$$\frac{h}{w_o} = \frac{d}{x} f(\alpha)\, g(\beta). \tag{1}$$

We excluded an explicit function of the convergence angle in Eq. (1) as the convergence angle in part determines the ratio $\beta$ (this is discussed below in Sec. IV B including Fig. 6).

Next, consider the length and width of the primary liquid sheet along the $x$-$z$ plane centered at $y = 0$. The sheet length, $l_j$, is the axial distance from the nozzle exit to the apex of the primary sheet. The sheet width, $w_j$, is the largest width of the primary sheet including the diameters of both rims at the edges. We hypothesized that the primary dynamics governing the relative scales of $l_j$ and $w_j$ is the competition between fluid inertia (expanding the sheet) and surface tension (acting to form the rims and redirect them toward the centerline). This hypothesis was first used by Taylor in the study of colliding jets of water. Due to water's relatively low viscosity (e.g., compared to the working fluids of Bush and Hasha), Taylor's sheets exhibited unstable rims, wherein liquid reaching the rims was ejected outward as droplets. Consequently, Taylor deduced the primary sheet shape simply by equating the z-direction inertial force with the surface tension: $\rho u_0^2 h = 2\sigma$ [2]. The latter approach suggests the following relation for primary sheet length; and a quantity referred to in Ref. [3] as the Taylor radius, $r_T$:

$$r_T(\phi) = \frac{\rho\, u_0 Q\,(\phi)}{2\,\sigma}. \tag{2}$$

Taylor's relation is equivalent to a constant Weber number based on sheet thickness at the sheet edge. Bush and Hasha showed that this relation does not hold well for sheet jets bound by thick rims because centripetal forces associated with the flow along the curved rim significantly influence the sheet shape and width. Bush and Hasha also noted that viscosity plays an important role in rim size and stability [3]. The latter idea suggests a capillary number dependence which we will introduce below.

## IV. RESULTS AND ANALYSES

### A. Jet observation

Figure 4 shows example images of liquid sheet jets generated by laminar streams through our converging nozzles with Reynolds numbers ($\mathrm{Re}_e$) of 74.8, 98.0, 1510, 526, and 554, with $\mathrm{Re}_e$ based on $d$ and nozzle exit bulk velocity. The flows are steady and form a "primary" (i.e., initial, largest) liquid sheet of roughly oval shape in the $x$-$z$ plane perpendicular to the largest dimension of the nozzle exit. Flow inertia tends to widen the sheet in the $x$-$z$ plane and surface tension results in the formation of relatively thick rims, and these rims limit the $z$-direction width of the sheet. Although all experiments were performed with the streamwise direction vertical, we estimate the effect of gravity was negligible and was omitted from our final analyses.

The dynamics can be described qualitatively as follows. The internal nozzle converges within the $x$-$y$ plane, creating two significant $y$-direction momentum fluxes opposing each other and flowing symmetrically toward the $y = 0$ plane. These two internal flow regions within the single nozzle are analogous to two free jets colliding at an oblique angle. As the jet exits the nozzle exit, the flow results in the formation of a sheet of liquid oriented in the $x$-$z$ plane and centered at about $y = 0$. This sheet spreads and widens symmetrically along the $z$ direction reducing the sheet "thickness" in the $y$ direction. Surface tension forces eventually dominate the outward fluid inertia limiting the $x$-$z$ dimensions of the sheet and causing the sheet to contract back toward the $x$-$y$ plane. The rim regions of the sheet recruit liquid from the sheet and grow as the sheet contracts back on itself eventually forming a downstream secondary sheet oriented in the $x$-$y$ plane. The flow, as shown in Fig. 4(a), can form a series of sheets of diminishing width and increasing thickness. Sheets are roughly oval and oriented alternately in the $x$-$z$ plane and the $x$-$y$ plane reminiscent of "fluid chain" structure

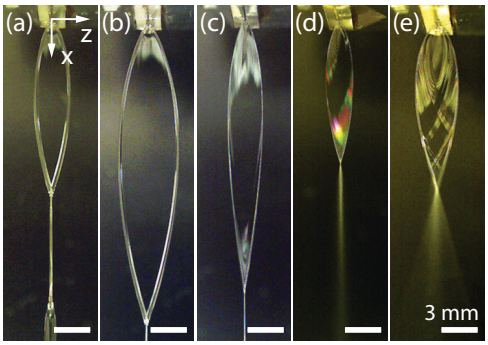


FIG. 4. Images of liquid sheet jets created using our microfluidic device. Images taken with optical axis perpendicular to first sheet jet (perspective shows some of the nozzle exit face). All the scale bars are 3 mm. Working liquids, flow rate, and nozzle dimensions of the experiments shown here are: (a) Mixture of ethylene glycol (80%, w/w) and water (20%, w/w): $Q = 42\,\mathrm{ml/min}$; $d = 125\,\mu\mathrm{m}$; $w_o = 1065\,\mu\mathrm{m}$; and $\theta = 75^\circ$. (b) Same as (a) except $Q = 55\,\mathrm{ml/min}$. (c) Ethanol: $Q = 21\,\mathrm{ml/min}$; $d = 125\,\mu\mathrm{m}$; $w_o = 152\,\mu\mathrm{m}$; and $\theta = 45^\circ$. (d) Ethanol: $Q = 6\,\mathrm{ml/min}$; $d = 38\,\mu\mathrm{m}$; $w_o = 125\,\mu\mathrm{m}$; and $\theta = 60^\circ$. (e) Water := $19\,\mathrm{ml/min}$; $d = 38\,\mu\mathrm{m}$; $w_o = 570\,\mu\mathrm{m}$; and $\theta = 75^\circ$.

categorized in Ref. [3] for colliding jets. As we increase the flow rate, the sheet formation is often interrupted by an instability which causes rapid dispersion of the sheet into a spray near the apex as shown in Figs. 4(d) and 4(e). If we increase the flow rate further, the instability propagates upstream. The former structure is likely analogous to respectively the "sheet with disintegrating rims" regime, and the latter to the "fishbone" regime categorized in Ref. [3]. The instability has been investigated and characterized as Rayleigh-plateau instability marked by capillary pinch-off of the fluid rims by Bush and Hasha and others [3,21]. The flow structures depicted in Fig. 4 are further described in the Supplemental Material [22].

We here selected flow conditions which result in the formation of sheet jets which can be characterized as either a classic "fluid chain" or "sheet with disintegrating rims." These regimes produced at least one primary sheet with little or no disintegration of the rim via flow instability, enabling accurate measurement of sheet thickness along the $x$ axis to a region near the downstream apex of the primary sheet (the location of minimum sheet thickness with along $z = 0$). The "fishbone" flow regime is less interesting for our applications and leads to strong instability and atomization. It is also less desirable to the applications discussed in the Introduction due to its associated higher, sample-consuming flow rates.

We obtained three sets of measurements of the primary sheet for each liquid jet: thickness ($h$) variation along the axial centerline as a function $x$, length ($l_j$), and width ($w_j$). The raw measurements obtained are shown in Figs. 6(a), 7(a), and 7(d). These data represent 401 measurements of averaged sheet thickness and 66 measurements of sheet length and width across 67 experimental conditions using 30 geometries and three working liquids. Thermophysical properties of the three liquids and the ranges of dimensionless numbers across the parameter variation for each liquid type are shown in Table I. Collectively, these variations in geometry, flow conditions, and liquids cover ranges of 0.56–15.4 $\mu$m, 5.4–32 mm, and 1.1–7.5 mm for $h$, $l_j$, and $w_j$ respectively. The thinnest sheet of 560 nm is shown in Fig. 4(d) and was achieved at $x = 9\,\mathrm{mm}$ using ethanol with a nozzle of $d = 38\,\mu\mathrm{m}$, $w_o = 125\,\mu\mathrm{m}$, and $\theta = 60^\circ$. For this case, the flow rate and the exit plane bulk velocity were 6 ml/min and 21.1 m/s, respectively. We also note that the nozzle geometry of Galinis *et al.* is significantly different than that of the current study, as it includes a short straight channel section immediately upstream of the nozzle exit plane and that the aspect ratio of their nozzle exit depth to width, $d/w_o$, is 8.7 compared to our respective depth-to-width ratios (relative to the first sheet) ranging from 0.067 to 0.82 [7].

TABLE I. Flow and fluid properties for experiments with three working liquids.

| | Ethanol | Water | Ethylene glycol-water mixture[a] |
|---|---|---|---|
| $\rho$ (kg/m$^3$) | 789 | 998 | 1100[b] |
| $\mu$ (Pa·s) | $1.20 \times 10^{-3}$ | $1.00 \times 10^{-3}$ | $9.66 \times 10^{-3}$[b] |
| $\sigma$ (N/m) | $22.4 \times 10^{-3}$ | $72.9 \times 10^{-3}$ | $53.0 \times 10^{-3}$[b] |
| $\mathrm{Re}_e$ | 173–1510 | 437–3820 | 74.7–399 |
| $\mathrm{We}_e$ | 322–3370 | 188–2510 | 609–3700 |
| $\mathrm{Ca}_e$ | 0.188–1.22 | 0.0578–0.420 | 1.10–5.15 |

[a]Mixture of ethylene glycol (80%, w/w) and water (20%, w/w).
[b]Fluid properties were taken from the measurements of Ref. [23].

### B. Scaling analyses

As for scaling $h$, we explored several forms of the functions $f(\alpha)$ and $g(\beta)$ in Eq. (1) and found very good collapse of jet thickness scaled data for

$$\frac{h}{w_o} = 0.35\frac{d}{x}(1 + 1.5\,\alpha^2)\beta^{-1}. \tag{3}$$

This scaling is shown in Fig. 6(b). A comparison of this result to a partial scaling based solely on $g(\beta)$ as shown in Fig. S1(b) demonstrates the efficacy of using $f(\alpha)$. The scaling of Eq. (3) is convenient that it relies only upon simulations of the internal flow of the device and does not rely on simulations of free surface flows or treatment of the effects of capillary forces of any kind.

Next, we strove to find a purely geometric scaling which would avoid simulations of the internal flow. To this end, we recognize that the ratio of streamwise to spanwise momentum flux in the case of colliding jets is simply cotangent of the collision angle. We thus hypothesized that $\beta$ would be solely expressed by a function of some effective nozzle convergence angle for our flow regimes of interest (including Reynolds numbers of 74.7 to 3820). As a result of the scaling shown in Fig. 5, we found the following relation based purely on the simulation data:

$$\beta^{-1} = 1 + \cot(0.67\theta). \tag{4}$$

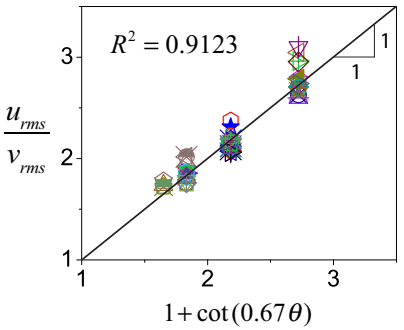


FIG. 5. Ratio of momentum-averaged streamwise velocity at the nozzle exit, $u_{\mathrm{rms}}$, to momentum-averaged spanwise velocity at the nozzle exit, $v_{\mathrm{rms}}$, as a function of convergence angle, $\theta$. The 0.67 prefactor was determined using linear regression, and the corresponding $R^2$ value is shown.

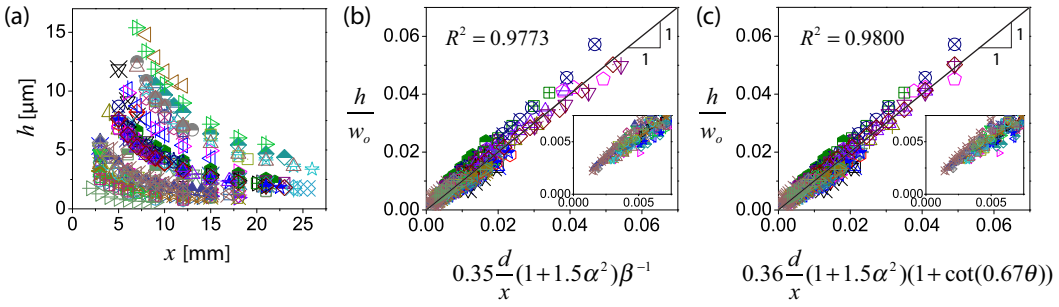


FIG. 6. Scaling of jet thickness of the primary sheet structure. Flow and geometric parameters of the data sets corresponding to the symbols are given in Table S1 of the Supplemental Material [22]. (a) Raw measured jet thickness, $h$, as a function of axial distance from nozzle exit, $x$. (b) Collapse of the scaled data onto a line with a slope of 1.0. (c) Collapse of the purely geometrically scaled data onto a line with a slope of 1.0. (b), (c) Prefactors were determined using linear regression, and the corresponding $R^2$ values are shown. The insets zoom the scaled data of minimum thickness. Larger format plots are displayed in the Supplemental Material to facilitate differentiating individual scaled data points [22].

We then simply replaced $\beta^{-1}$ with $1 + \cot(0.67\theta)$ in Eq. (3), which led us to the following scaling with the prefactor determined by linear regression:

$$\frac{h}{w_o} = 0.36\,\frac{d}{x}(1 + 1.5\,\alpha^2)\,[1 + \cot(0.67\theta)]. \tag{5}$$

Figure 6(c) shows the result of this scaling theory, which is based purely on the geometry of the device and no flow quantities (despite our flows' Reynolds numbers of up to roughly 4,000). As shown in Fig. 5, the function of $\theta$ cannot capture the change of momentum flux ratio due to the variance of nozzle depth, $d$, and exit width, $w_o$. Nevertheless, the collapse of the scaled data is as successful as that of Fig. 6(b) (to within errors of measurement). The scaling result predicts jet sheet thickness as a function of the coordinate $x$ based purely on the geometry of the nozzle with no need for fluid mechanics simulations. We believe this scaling is therefore the most useful to the planning and fabrication of sheet jets in the 1 to 10 $\mu$m region (and even a factor of 2 on either side). We caution that our work validates our scaling only within the parameters explored (including Reynolds numbers of 74.7–3820, aspect ratios of 0.067–0.82, and convergence angles between 45° and 85°). Figure S6 shows the scaled minimum thickness data per each data set to facilitate identifying minimal thickness associated with control parameters [22].

For scaling $l_j$ and $w_j$, we first attempted to scale $l_j$ using a Weber number based on a jet thickness at the apex of the primary sheet, $h_v$. However, our sheet jets often either formed thick rims colliding at the apex or were unstable with disintegrating rims, and this made quantification of $h_v$ difficult. This led us to estimate $h_v$ simply using the value suggested by our scaling analysis, namely, Eq. (3), so that

$$h_v = h_{x=l_j} = 0.35\,\frac{d w_o}{l_j}\,\frac{u_{\mathrm{rms}}}{v_\alpha}, \tag{6}$$

where $v_\alpha = v_{\mathrm{rms}}(1 + 1.5\,\alpha^2)^{-1}$. Following Taylor's idea of Eq. (2), we here hypothesize a scaling of a constant Weber number expressed in terms of the minimum sheet thickness of Eq. (6) and $v_\alpha$, $\mathrm{We}_j = \rho v_\alpha^2 h_v / \sigma$. Given this scaling, we found a good collapse of the data as shown in Fig. S2 [22] for

$$\mathrm{We}_j = 0.88. \tag{7}$$

In the case of colliding jets, the radial distribution of momentum flux is primarily a function of diameter of the colliding jets, impact angle, and azimuthal angle. These parameters determine

the planar oval shape of the primary sheet including its major and minor axes. In an analogy to this, we attempt to relate the ratio of width to length of the primary sheet, $\gamma = w_j/l_j$, to the ratio of spanwise to streamwise momentum flux and a function of $\alpha$ describing the initial shape of the stream leaving the nozzle exit. Consequently, we hypothesized a power-law scaling of the form $\gamma = \mathrm{We}_j\,(1 + 1.5\alpha^2)^m \beta^n$ and found a very good collapse of scaled width data of the form

$$\gamma = 0.58\ \mathrm{We}_j \beta\,(1 + 1.5\,\alpha^2)^{-1} = 0.58\ \mathrm{We}_j \beta_\alpha, \tag{8}$$

as shown in Fig. S3 [22] where $\beta_\alpha = v_\alpha/u_{\mathrm{rms}} = \beta\,(1 + 1.5\,\alpha^2)^{-1}$.

The simple forms of the scaling results of Eqs. (7) and (8) are helpful in developing an intuitive understanding of the phenomena and comparing the current results to those of Taylor. However, in the forms shown above, the scalings are a rather inconvenient way to directly relate and calculate $l_j$ and $w_j$ to the controlling geometrical and flow rate parameters. We also assert it is more convenient to replace $\beta$ with the aforementioned function of theta and have the scaling not rely on full Navier-Stokes calculation of the internal nozzle flow. To this end, we proposed a scaling in terms of a Weber number based on the $y$-direction thickness of the stream at $x = 0$, and the nozzle outlet dimension $w_o$ as $\mathrm{We}_e = \rho Q^2/\sigma d^2 w_o$. Combining Eqs. (7) and (8) with (4), (5), and $\bar{u} \approx u_{\mathrm{rms}}$ (see the Supplemental Material including Fig. S4 for further details [22]) and determining prefactors based on linear regression, we then have

$$\frac{l_j}{d} = 0.36\ \mathrm{We}_e\,(1 + 1.5\,\alpha^2)^{-1}[1 + \cot(0.67\theta)]^{-1} \tag{9}$$

and

$$\frac{w_j}{d} = 0.17\ \mathrm{We}_e\,(1 + 1.5\,\alpha^2)^{-2}[1 + \cot(0.67\theta)]^{-2}. \tag{10}$$

The scaling of Eqs. (9) and (10) is purely determined by geometric parameters and the flow rate-dependent Weber number at the nozzle exit (hence does not require details of the velocity field). As shown in Figs. 7(b) and 7(e), these scalings well collapse the length and width data and have the benefit of explicit relations for each quantity obviating a need for CFD simulations of internal flow.

Last, we note the poor collapse of jet length and width data for high values of the abscissa in Figs. 7(b) and 7(e). We hypothesized that viscosity plays an important role in for these relatively high Weber number regimes and thus introduced a scaling based on a capillary number of the form $\mathrm{Ca}_e = \mu Q/\sigma d w_o$. This led to a modification of the scaling Eqs. (9) and (10) as follows:

$$\frac{l_j}{d} = 0.23\ \mathrm{We}_e\,\mathrm{Ca}_e^{-0.1}(1 + 1.5\,\alpha^2)^{-0.5}[1 + \cot(0.67\theta)]^{-0.5} \tag{11}$$

and

$$\frac{w_j}{d} = 0.074\ \mathrm{We}_e\,\mathrm{Ca}_e^{-0.2}(1 + 1.5\,\alpha^2)^{-1}[1 + \cot(0.67\theta)]^{-1}. \tag{12}$$

Although more complex, Figs. 7(c) and 7(f) show significant improvement of the collapse of scaled data across the full range, particularly for the data for sheet jets with varying dynamic viscosities. Again, note this requirement for $\mathrm{Ca}_e$ scaling is consistent with the observations of Bush and Hasha who pointed out the importance of fluid viscosity in stabilizing the rim structures of the jet, and the interplay between sheet surface tension and the centripetal forces on these sheet rims [3]. We stress that the scaling Eqs. (9)–(12) in prediction of primary sheet length and width are based solely on the nozzle geometry, flow rate, and thermophysical fluid properties without a need for CFD simulations of internal flow.

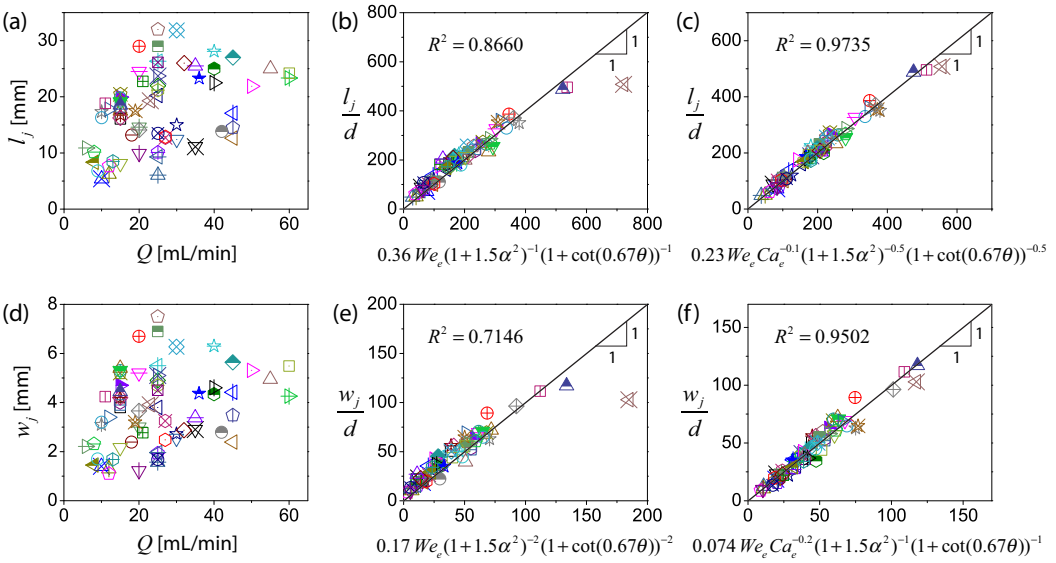


FIG. 7. Scaling of length and width of the primary sheet. Flow and geometric parameters of the data sets corresponding to the symbols are given in Table S1 of the Supplemental Material [22]. (a), (d) Measurements of the primary sheet length, $l_j$, and width, $w_j$, respectively, as a function of flow rate, $Q$. (b), (e) Partial collapse of respective sheet length and width scaled solely with $\mathrm{We}_e$ without taking viscosity into account onto a line with a slope of 1.0, respectively. (c), (f) Strong collapse of respective sheet length and width fully scaled with both $\mathrm{We}_e$ and $\mathrm{Ca}_e$ onto a line with a slope of 1.0, respectively. (b)–(f) Prefactors were determined using linear regression, and the corresponding $R^2$ values are shown in each plot. Larger format plots are displayed in the Supplemental Material to facilitate differentiating individual scaled data points [22].

## V. CONCLUSIONS

We introduced a planar design of converging nozzles convenient for generation of liquid sheet jets with sheet thicknesses from tens of micron to submicron. The smallest sheet thickness we measured was 560 nm. However, we hypothesize that significantly thinner sheets can be achieved by reducing channel dimensions. For example, our scaling analysis suggests that nozzle exit dimensions of $d = 20\,\mu$m, $w_o = 40\,\mu$m with $\theta = 60^\circ$ would still be practical for many liquid solutions and would generate sheets 250 nm-thick at a distance $50\,\mu$m from the apex of a 3 ml/min water sheet. We summarized the results of detailed experimental parametric studies and scaling analyses for the jet structures. Drawing insights from classic studies of colliding jets, we hypothesized scaling theories for jet thickness, length, and width of primary sheets. For sheet thickness, we first presented a scaling based on nozzle geometry and CFD calculations of momentum fluxes at nozzle exit. We then presented a scaling based purely on nozzle geometry which obviates the need for detailed computational fluid dynamics calculations. The scaling theory showed excellent collapse of the scaled data for our parametric variations including Reynolds number of 74.7–3820. We believe that the latter scaling theory would be most useful in prediction of jet thickness as a function of $x$ coordinate and thus the jet design as well. For sheet length and width, we leveraged the idea that the ratios of sheet length and width to nozzle depth are governed primarily by the competition between fluid inertia and surface tension, and to a lesser degree by the effects of viscosity. We proposed two associated scaling theories. The first is based on Weber number and nozzle geometry, and the second on Weber number, capillary number, and nozzle geometry. The latter demonstrated better collapse of scaled data, strongly implying viscosity plays a role in limiting sheet jet development for the thinnest sheets. Both scaling theories are based on flow rate and thermophysical fluid

properties and do not require computation of the internal flow. Together the fabrication method and scaling theories provide useful design rules for the design and application of liquid sheet jets.

**ACKNOWLEDGMENT**

This research used the resources of SLAC National Accelerator Laboratory, supported by the U.S. Department of Energy, Office of Science, Office of Basic Energy Sciences under Contract No. DE-AC02-76SF00515.

[1] N. Dombrowski and R. P. Fraser, A photographic investigation into the disintegration of liquid sheets, Philos. Trans. R. Soc. A **247**, 101 (1954).
[2] G. I. Taylor, Formation of thin flat sheets of water, Proc. R. Soc. Lond. A **259**, 1 (1960).
[3] J. W. Bush and A. E. Hasha, On the collision of laminar jets: Fluid chains and fishbones, J. Fluid Mech. **511**, 285 (2004).
[4] C. Clanet, Waterbells and liquid sheets, Annu. Rev. Fluid Mech. **39**, 469 (2007).
[5] M. Kondoh and M. Tsubouchi, Liquid-sheet jets for terahertz spectroscopy, Opt. Express **22**, 14135 (2014).
[6] M. Ekimova, W. Quevedo, M. Faubel, P. Wernet, and E. T. Nibbering, A liquid flatjet system for solution phase soft-x-ray spectroscopy, Struct. Dyn. **2**, 054301 (2015).
[7] G. Galinis, J. Strucka, J. C. Barnard, A. Braun, R. A. Smith, and J. P. Marangos, Micrometer-thickness liquid sheet jets flowing in vacuum, Rev. Sci. Instrum. **88**, 083117 (2017).
[8] M. J. Tauber, R. A. Mathies, X. Chen, and S. E. Bradforth, Flowing liquid sample jet for resonance Raman and ultrafast optical spectroscopy, Rev. Sci. Instrum. **74**, 4958 (2003).
[9] A. Watanabe, H. Saito, Y. Ishida, M. Nakamoto, and T. Yajima, A new nozzle producing ultrathin liquid sheets for femtosecond pulse dye lasers, Opt. Comm. **71**, 301 (1989).
[10] A. Ghazal, J. P. Lafleur, K. Mortensen, J. P. Kutter, L. Arleth, and G. V. Jensen, Recent advances in x-ray compatible microfluidics for applications in soft materials and life sciences, Lab Chip **16**, 4263 (2016).
[11] M. Fondell *et al.*, Time-resolved soft x-ray absorption spectroscopy in transmission mode on liquids at MHz repetition rates, Struct. Dyn. **4**, 054902 (2017).
[12] J. D. Koralek *et al.*, Generation and characterization of ultrathin free-flowing liquid sheets, Nat. Comm. **9**, 1353 (2018).
[13] J. Klebniczki, J. Hebling, B. Hopp, G. Hajos, and Z. Bor, Fluid jet with variable thickness in the range 5–20 μm, Meas. Sci. Technol. **5**, 601 (1994).
[14] D. E. Hertzog, B. Ivorra, B. Mohammadi, O. Bakajin, and J. G. Santiago, Optimization of a microfluidic mixer for studying protein folding kinetics, Anal. Chem. **78**, 4299 (2006).
[15] S. Kedenburg, M. Vieweg, T. Gissibl, and H. Giessen, Linear refractive index and absorption measurements of nonlinear optical liquids in the visible and near-infrared spectral region, Opt. Mater. Express **2**, 1588 (2012).
[16] E. Sani and A. Dell'Oro, Optical constants of ethylene glycol over an extremely wide spectral range, Opt. Mater. **37**, 36 (2014).
[17] F. M. White and I. Corfield, *Viscous Fluid Flow* (McGraw-Hill Higher Education, Boston, 2006), Vol. 3.
[18] K. D. Miller, Jr., Distribution of spray from impinging liquid jets, J. Appl. Phys. **31**, 1132 (1960).
[19] D. Hasson and R. E. Peck, Thickness distribution in a sheet formed by impinging jets, AIChE J. **10**, 752 (1964).
[20] E. A. Ibrahim and A. J. Przekwas, Impinging jets atomization, Phys. Fluids A **3**, 2981 (1991).
[21] S. Jung, S. D. Hoath, G. D. Martin, and I. M. Hutchings, Atomization patterns produced by the oblique collision of two Newtonian liquid jets, Phys. Fluids **22**, 042101 (2010).

[22] See Supplemental Material at http://link.aps.org/supplemental/10.1103/PhysRevFluids.3.114202 for summary of nomenclautre, tabulated summary of all the data sets corresponding to each data symbol, and further details concerning the experiments and the scaling methods and results.

[23] N. G. Tsierkezos and I. E. Molinou, Thermodynamic properties of water+ethylene glycol at 283.15, 293.15, 303.15, and 313.15 K, J. Chem. Eng. Data **43**, 989 (1998).